



Heterogeneous Microstructure-Induced Mechanical Responses in Various Sub-Zones of EH420 Shipbuilding Steel Welded Joint Under High Heat Input Electro-Gas Welding

Xu Xie¹ · Tan Zhao² · Heming Zhao³ · Song Li⁴ · Cong Wang^{1,5}

Received: 22 January 2021 / Revised: 16 March 2021 / Accepted: 17 March 2021 / Published online: 6 May 2021
© The Chinese Society for Metals (CSM) and Springer-Verlag GmbH Germany, part of Springer Nature 2021

Abstract

Heterogeneous microstructure-induced mechanical responses in EH420 shipbuilding steel welded joint by electro-gas welding processed have been systematically studied by scanning electron microscopy, electron backscatter diffraction and mechanical testing. Comparing with the coarse-grained heat-affected zone (CGHAZ), the weld metal presents higher toughness (129.3 J vs. 37.3 J) as it contains a large number of acicular ferrites with high-angle grain boundaries (frequency 79.2%) and special grain boundary $\Sigma 3$ (frequency 55.3%). Moreover, coarse austenite grains in CGHAZ and slender martensite–austenite constituents between bainite laths may likely facilitate crack propagation. Polygonal ferrites and tempered pearlites formed at the junction of the fine-grained heat-affected zone and the intercritical heat-affected zone induced a softened zone with an average hardness of 185 HV0.5, which is the main reason for the occurrence of tensile fracture.

Keywords Heterogeneous microstructure · Mechanical properties · Electro-gas welding · High heat input · Shipbuilding steel

1 Introduction

In the shipbuilding industry, high deadweight ships demand thicker steel plates to be used in the hull structure [1]. However, such thicker steel plates require multi-pass welding in the manufacturing process, which will reduce productivity and, invariably, lead to unexpected costs [2]. In practice, to avoid such scenario, traditional multi-pass welding technology has been gradually replaced by high heat input welding

techniques [2–5]. It is worth noting that welds in certain vertical positions usually adopt electro-gas welding (EGW) to achieve single-pass welding with high heat input [2].

EH420 shipbuilding steel is a typical high-strength low-alloy (HSLA) steel for hull structure applications, which have markedly cryogenic toughness and excellent weldability [6, 7]. In particular, EGW is widely adopted to join EH420 shipbuilding steel. Under high heat input welding conditions, high peak temperature and extended duration for temperature drop-off may induce coarse austenite grains and heterogeneous microstructure formation such as acicular ferrite, lath bainite, ferrite side plate, grain boundary ferrite, polygonal ferrite and martensite–austenite (M–A) constituents in the heat-affected zone (HAZ), resulting in deteriorated mechanical properties and potentially reduced safety performance during service [6, 8–16]. In addition, various phases in the heterogeneous microstructure exhibit different crystallographic characteristics, which may also impart non-uniform mechanical properties, especially cryogenic toughness [14, 17–20]. It has been reported that the special grain boundary $\Sigma 3$, belonging to a type of the coincident site lattice, can effectively suppress crack propagation [21–23].

Tremendous effort has been made to clarify heterogeneous microstructures in different sub-zones of welding joints

Available online at <http://link.springer.com/journal/40195>.

✉ Cong Wang
wangc@smm.neu.edu.cn

- ¹ School of Metallurgy, Northeastern University, Shenyang 110819, China
- ² State Key Laboratory of Metal Material for Marine Equipment and Application, Angang Steel Co., Ltd., Anshan 114021, China
- ³ Minmetals Yingkou Medium Plate Co., Ltd., Yingkou 115005, China
- ⁴ Nanjing Steel Co., Ltd., Nanjing 210035, China
- ⁵ State Key Laboratory of Rolling and Automation, Northeastern University, Shenyang 110819, China

caused non-uniform mechanical properties in HSLA steel during high heat input [12, 24, 25]. Shen et al. [17] investigated microstructure changes of 12MnNiVR pressure vessel steel processed after high heat input EGW and found that heterogeneous microstructures with various crystallographic features were exhibited in both the coarse-grained heat-affected zone (CGHAZ) and the fine-grained heat-affected zone (FGHAZ). It was pointed out that coarse austenite grain sizes (51.7 μm) and low frequency of HAGBs (38.7%) contributed to deteriorated strength and toughness in CGHAZ. Zou et al. [6] revealed, with high heat input exceeding 100 kJ/cm, that the microstructure transformed from lath bainite to coarse granular bainite and acicular ferrite by simulating the CGHAZ of EH420 shipbuilding steel, which could cause various grain boundary misorientation and might induce different mechanical responses. Lan et al. [11, 26] indicated that large-sized M-A components, harder than adjacent metals, could promote cleavage crack growth in the CGHAZ of a low-carbon bainitic steel. Di et al. [27, 28] indicated, for thicker bainite steel, that the heterogeneous microstructures, composed of martensites and tempered bainites, could also be enabled by the partial $\alpha \rightarrow \gamma$ transformation in the simulated intercritical heat-affected zone (ICHAZ), which may likely be the main factors for toughness reduction.

It is noteworthy that most of the available studies are focused on specific sub-zones in HAZ, while few pay attention to the relationship between heterogeneous microstructure and mechanical properties in the entire welded joint. The present paper is poised to reveal the evolution of heterogeneous microstructure and crystallographic characteristics in various sub-zones of EH420 shipbuilding steel welded joint during high heat input and to explore heterogeneous microstructure-induced mechanical responses by quantitative characterization of grain sizes and the frequency of grain boundaries in different sub-zones.

2 Experimental

EH420 shipbuilding steel treated by thermo-mechanically controlled processing (TMCP) was used as the experimental material. Two identical dimensions of 600 mm (length) \times 150 mm (width) \times 30 mm (thickness) were welded together by a 30° V-type groove, and the welding direction was perpendicular to the rolling direction. The welding parameters for the single-pass filling V-type groove were: welding current 390 A, arc voltage 39 V, welding speed 6.42 cm/min, and heat input 142.1 kJ/cm. The welding filling material was made

of DW-S1LG welding wire with a diameter of 1.6 mm, and the shielding gas during the welding process was pure CO_2 . Chemical compositions of EH420 shipbuilding steel and the weld metal (WM) are shown in Table 1.

Figure 1 shows the different locations of the test specimens cut from the weldment. Microstructure characterization was observed by cutting a metallographic sample from a cross-sectional welded plate perpendicular to the welding direction. The mechanically polished sample was etched by 4% Nital for microstructure observation. The microstructure was revealed by scanning electron microscopy (SEM, TESCAN, MAIA3XMH, CZ) at an acceleration voltage of 20.0 kV. Energy-dispersive spectrometry (EDS) was used to analyze the composition of typical inclusions in the weld metal. In addition, crystallographic features at different sub-zones of the welded joint were characterized using

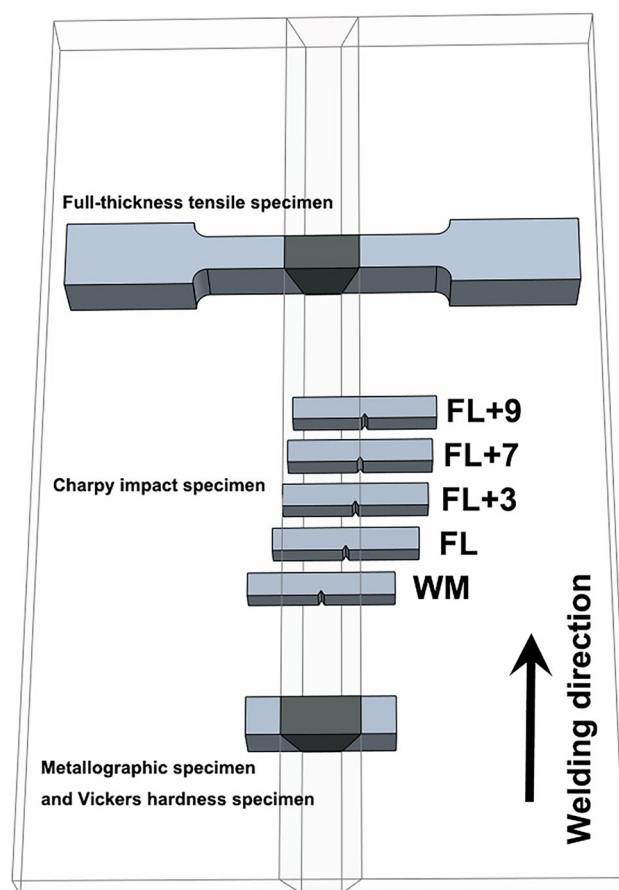


Fig. 1 Schematic illustrations of the different test specimen locations from the weldment

Table 1 Chemical compositions of the EH420 steel plates and WM (wt%)

| Materials | C | Si | Mn | Ni | P | Mg | Ti | Al | S | O |
|-----------|-------|------|------|------|-------|--------|-------|-------|-------|-------|
| EH420 | 0.052 | 0.13 | 1.66 | 0.32 | 0.011 | <0.001 | 0.010 | 0.003 | 0.006 | 0.002 |
| WM | 0.042 | 0.16 | 1.73 | 1.48 | 0.011 | 0.001 | 0.020 | 0.005 | 0.007 | 0.028 |

electron backscattered diffraction (EBSD) analysis with the sample dimension of 18 mm × 4 mm × 0.4 mm. The sample was electropolished by a mixed solution of perchloric acid and alcohol (volume ratio 1:20). Corresponding parameters were: operating voltage 20.0 kV, sample stage tilted 70°, working distance 15 mm and scanning step 0.45 μm.

Mechanical properties of the welded joint were determined by Vickers hardness, Charpy impact tests and full-thickness tensile tests. The hardness was measured on an HXD-1000 microhardness tester with a load of 0.5 kgf and a step of 250 μm. The central area of the full-thickness steel plate was selected as the hardness test zone, and the hardness values of ten straight lines were measured in the specified area [17]. The Charpy impact test protocol was designed according to the ASTM A370 standard. The sample dimensions were 10 mm × 10 mm × 55 mm. The sample V-notch positions were machined at WM, the fusion line (FL), 3 mm from the FL (at CGHAZ), 7 mm from the FL (at FGHAZ) and 9 mm from the FL (at ICHAZ), which are named as WM, FL, FL + 3, FL + 7, FL + 9, respectively, as shown in Fig. 1. Each position was tested three times, and the average value was used as the result. Charpy impact tests were performed on a SANS-ZBC2452-C pendulum impact tester at 233 K. Three full-thickness tensile tests were performed on a standard tensile specimen of the welded joint using a 600-kN tensile testing machine (KRDW-600G, Kairui, China) at room temperature, and the average value of three tests was reported. Fractography of fractured Charpy impact specimens and full-thickness tensile specimens was observed and documented by SEM at conditions mentioned above.

3 Results and Discussion

3.1 Hardness Distributions

Figure 2 shows the Vickers hardness distributions at different sub-zones of the welded joint. The hardness test zone is marked in the white rectangle in the inset of Fig. 2. From the weld center line to the BM, it can be seen that five distinct regions can be divided according to hardness magnitudes. In the WM, the hardness distribution is high and uniform with an average value of 237 HV0.5. The reason why the hardness of the WM is higher than that of other regions could be likely related to the filling material [29–31]. In the HAZ, the hardness distribution tends to decrease at first and then increase as the distance from the fusion line increases. From the CGHAZ to the FGHAZ, the hardness value gradually decreases from 230 HV0.5 to 185 HV0.5. In the ICHAZ close to the BM, the hardness distribution gradually approaches the BM until it becomes equivalent to 221 HV0.5. Meanwhile, it is worth noting that the softened zone of the welded joint occurs at the junction of the

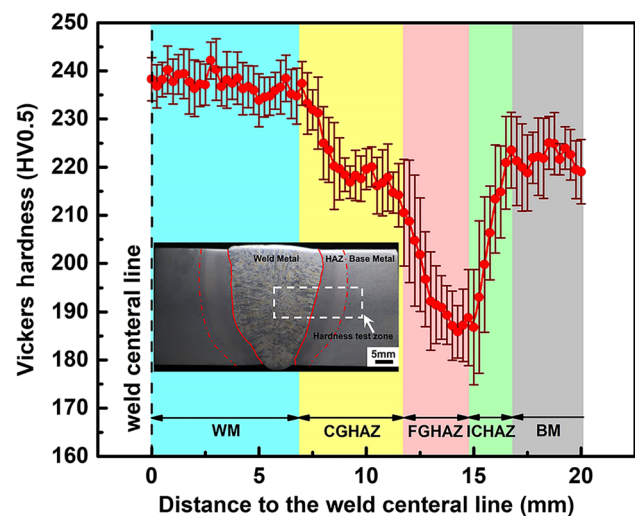


Fig. 2 Vickers hardness distributions of the welded joint. (Inset is a macrograph of EH420 shipbuilding steel welded joint)

FGHAZ and ICHAZ. The distinctly non-uniform hardness distribution in the welded joint is mainly due to the heterogeneous microstructure in different sub-zones, which will be discussed later.

3.2 Microstructures

Figure 3 illustrates SEM micrographs at different sub-zones of the welded joint. Figure 3a shows acicular ferrites, polygonal ferrites and M–A constituents in the WM. M–A constituents are mainly precipitated between acicular ferrites and carry polygonal morphology, as shown in the right top inset of Fig. 3a. Ti–Al–Mg–Mn–S–O complex inclusions are formed in the WM, as shown in the left bottom inset of Fig. 3a, which could effectively promote acicular ferrite nucleation [11, 29]. Figure 3b presents the detailed microstructure of lath bainite, granular bainite and M–A constituents in the CGHAZ. Interestingly, slender M–A constituents are found among between the lath bainite boundaries, as shown in the right top inset of Fig. 3b. The heterogeneous microstructure of the lath bainite and M–A constituents may bring a slight increase in hardness compared with that of the BM [32]. Microstructures in the FGHAZ are mainly polygonal ferrite, pearlite and M–A constituents (Fig. 3c). Finely carburized and layered pearlite structures and irregular M–A constituents at the polygonal ferrite boundary are shown in the left bottom and right top inset of Fig. 3c, respectively. As shown in Fig. 3d, the microstructure is mainly composed of polygonal ferrites, bainite, and M–A constituents in the ICHAZ. Newly formed M–A constituents are clearly shown along the grain boundaries in the right top inset of Fig. 3d. In addition, microstructures of the BM are characterized by fine polygonal ferrites and bainites enabled by TMCP (Fig. 3e).

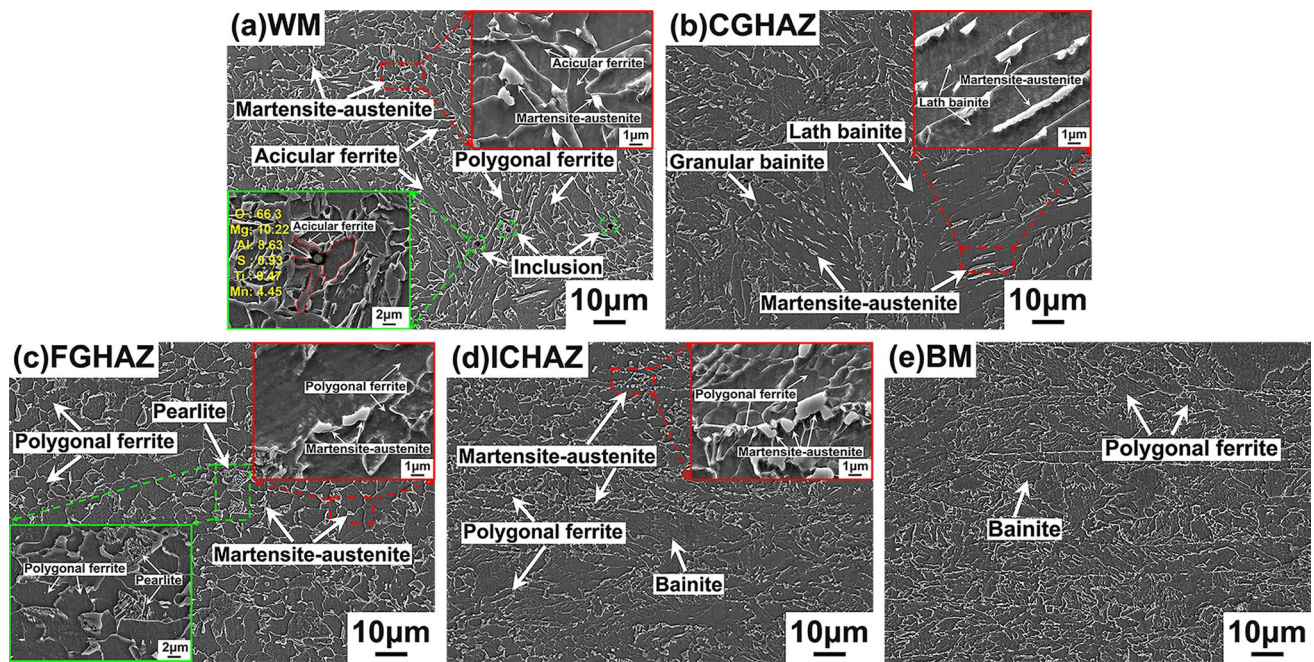


Fig. 3 SEM micrographs showing typical microstructures of EH420 shipbuilding steel welded joint: **a** WM; **b** CGHAZ; **c** FGHAZ; **d** ICHAZ; **e** BM

3.3 Crystallographic Characteristics

Figure 4 illustrates detailed EBSD mappings at different sub-zones of the welded joint. Figure 4a shows the randomly distributed acicular ferrites, which have different crystal orientations and are interlocked with each other in the WM. In the CGHAZ (Fig. 4b), the parallel-arranged bainite laths inside coarse prior austenite grains (PAGs) exhibit identical crystal orientations. As shown in Fig. 4c, fine polygonal ferrites in the FGHAZ exhibit various crystal orientations, and the orientation variations are large enough between adjacent grains. Regarding the ICHAZ in Fig. 4d, the original polygonal ferrites become coarse during the welding thermal cycle, which exhibit similar crystal orientations. It is worth noting that sizable amount of fine polygonal ferrites in the ICHAZ have not undergone discernable phase transformation, which still present varied crystal orientations [28].

Corresponding grain boundary distributions at different sub-zones of the welded joint are illustrated in Fig. 4e–h. The misorientation angle more than 10° is defined as high-angle grain boundaries (HAGBs), while the misorientation angle less than 10° is termed as low-angle grain boundaries (LAGBs) [33]. The acicular ferrite grains in WM mostly exhibit HAGBs with a frequency of 71.8%, while other microstructures show LAGBs with a frequency of 28.2%, as shown in Fig. 4e. In the CGHAZ, the misorientation angle boundaries of PAGs are HAGBs, whereas the mutually parallel bainite laths within PAGs, exhibiting low misorientations, can be classified as LAGBs, as shown in Fig. 4f.

Relative frequency of LAGBs in the CGHAZ is 76.9%, while that of HAGBs is 23.1%. In Fig. 4g, it can be seen that polygonal ferrites in the FGHAZ show a high frequency (83.3%) of HAGBs, while pearlites at the polygonal ferrite boundary exhibit a low frequency (16.7%) of LAGBs. In the ICHAZ, the original polygonal ferrites still exhibit HAGBs with the frequency of 42.4%, but large numbers of LAGBs (57.6%) are dispersed in their interior due to the existence of the sub-grain boundaries (Fig. 4h) [28]. Figure 4i–l shows special grain boundary distribution maps at different sub-zones of the welded joint. Special grain boundary $\Sigma 3$ are represented by yellow lines. According to statistical analysis, the frequency of $\Sigma 3$ is 55.3% for WM, 37.7% for CGHAZ, 45.7% for FGHAZ and 19.6% for ICHAZ, respectively.

3.4 Strength and Toughness

Figure 5a shows the stress–strain curve of the full-thickness tensile test over the welded joint. The yield strength, ultimate tensile strength and elongation of the welded joint are 527.6 ± 18.6 MPa, 625.8 ± 15.4 MPa and $23.7 \pm 1.7\%$, respectively. The fracture position of the tensile specimen is at the junction of FGHAZ and ICHAZ, and apparent necking phenomenon may have occurred upon fracturing, as shown in the middle inset of Fig. 5a. The fractured surface morphology of the tensile specimen exhibits a large number of randomly distributed fine and shallow dimples and cleavage faces, as shown in the bottom inset of Fig. 5a, which

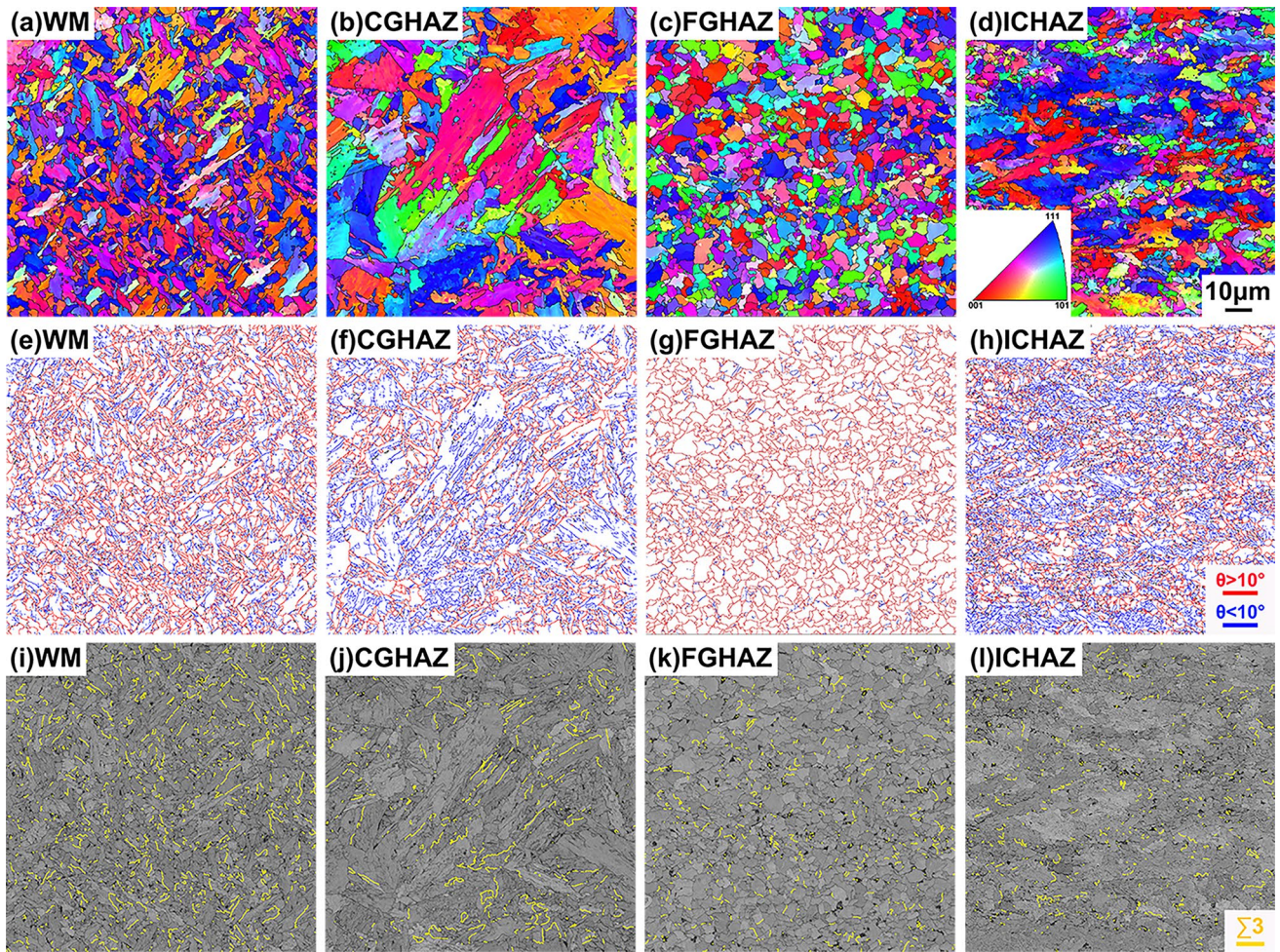


Fig. 4 Crystallographic characteristics of EH420 shipbuilding steel at different sub-zones of the welded joint: **a–d** orientation image maps; **e–h** grain boundaries distribution maps; **i–l** special grain boundary $\Sigma 3$ distribution maps (red lines represent HAGBs above 10° ; blue lines represent LAGBs of 2° – 10° ; yellow lines represent special grain boundary $\Sigma 3$)

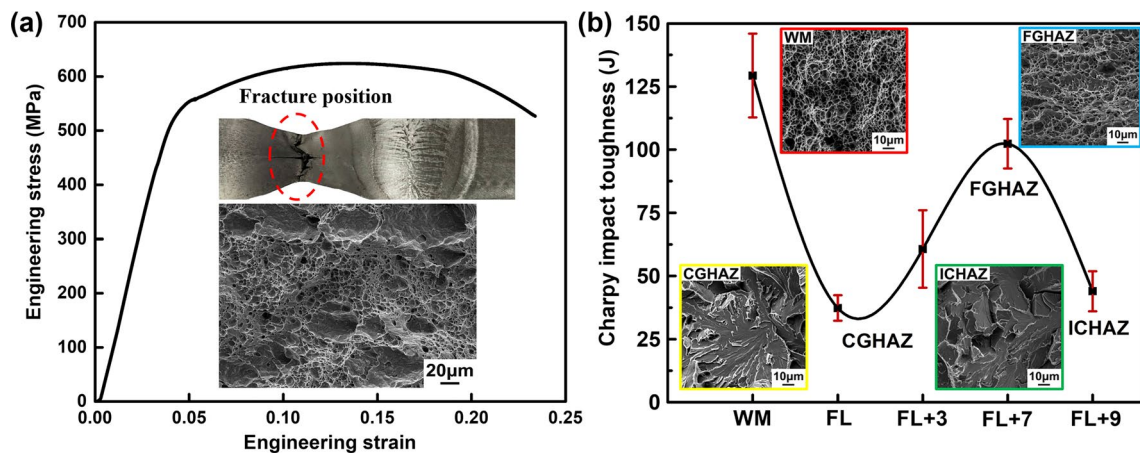


Fig. 5 Mechanical properties of the welded joint: **a** full-thickness tensile test results; **b** Charpy impact toughness results at different sub-zones

represents typical quasi-cleavage characteristics of brittle and ductile mixed fracture.

Figure 5b shows Charpy impact toughness values and morphologies of the fractured surface at different sub-zones of the welded joint. According to hardness distribution, the positions of FL and FL + 3 are located in CGHAZ. The impact toughness values of the WM (129.3 ± 16.6 J) and FGHAZ (102.3 ± 9.8 J) are higher, while the values of the CGHAZ (37.3 ± 5 J) and ICHAZ (44 ± 7.9 J) are appreciably lower. As shown in Fig. 5b, corresponding morphologies of the WM (red inset) and FGHAZ (blue inset) show a large number of fine and deep dimples. Such dimples coalesce with each other to form micro-void bands, which can effectively increase energy absorption during crack propagation [8, 12]. However, morphologies of the fractured surface in the CGHAZ and ICHAZ indicate typical quasi-cleavage features with a mixed brittle and ductile fracture mode, as shown by the yellow and green insets in Fig. 5b. In addition, ductile fracture bands are randomly distributed between adjacent cleavage facets. Cleavage facets can hardly prevent crack propagation, while ductile fracture bands may effectively promote crack deflection and suppress crack propagation [8, 32].

Under high heat input welding conditions, complex thermal cycle process may likely usher in heterogeneous microstructures and crystallographic features in different sub-zones of the welded joint [12]. Schematic illustrations of heterogeneous microstructural variation in different sub-zones of the welded joint are shown in Fig. 6. Randomly interlocking distributed acicular ferrites in WM, with fine grains (average grain sizes of 3 ± 1 μm) and high frequency of the HAGBs (71.8%) and special grain boundary $\Sigma 3$ (55.3%), owing to different crystal orientations, show a highly heterogeneous structure (Fig. 6b) [14, 34]. Normally, grain size refinement, high-frequency HAGBs, and $\Sigma 3$ can effectively improve toughness [34]. In

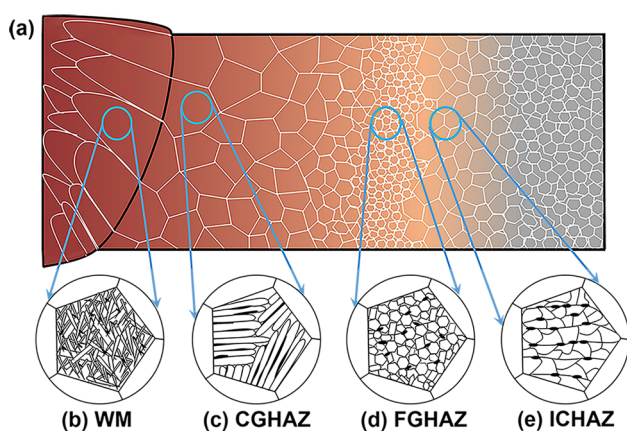


Fig. 6 Schematic illustrations of heterogeneous microstructural variation: **a** entire welded joint; **b** acicular ferrites in WM; **c** lath bainites in CGHAZ; **d** FGHAZ; **e** ICHAZ

addition, effective Ti–Al–Mg–Mn–S–O complex inclusions in the WM promote the formation of acicular ferrites, which, in turn, may obstruct the propagation of microcracks [35, 36]. As shown in Fig. 6c, high peak temperature and longer soaking time result in the microstructures of the BM transformed into coarse PAGs (average grain sizes of 49 ± 4 μm) in the CGHAZ, and the mutually parallel bainite laths within PAGs exhibit the same crystal orientation, representing a lowly mixed structure, which possesses low-frequency HAGBs (23.1%) and $\Sigma 3$ (37.7%). Therefore, the crack propagation may pass through parallel bainite laths without path deflection [37, 38]. Finely polygonal ferrites in FGHAZ, with fine grain sizes (average grain sizes of 8 ± 1 μm) and high-frequency HAGBs (83.3%) and $\Sigma 3$ (45.7%), show different crystal orientations and represent a highly mixed structure (Fig. 6d). The fine microstructure is the main reason for improved ductility and toughness in this region. In the ICHAZ (Fig. 6e), relatively low peak temperature and transitory soaking time lead to the partial transformations of the microstructure, forming coarse polygonal ferrites with identical crystal orientation [28]. Simultaneously, the heterogeneous microstructure at the junction of FGHAZ and ICHAZ undergoes a high-temperature tempering transformation. The original ferrite and bainite are austenitized firstly, and then, austenite transforms into polygonal ferrite and tempered pearlite due to the small undercooling under high heat input, forming a softened zone, which is the main reason for the occurrence of tensile fracture [7, 14, 28].

In addition, the shape and distribution of M–A constituents in different sub-zones are also decisive factors affecting crack propagation [26, 31, 37]. M–A constituents are characterized by the slender shape (average grain sizes of 5 ± 3 μm) in the CGHAZ, but may exhibit polygonal morphology (average grain sizes of 2 ± 1 μm) in other sub-zones, as shown in Fig. 3a–d. Compared with polygonal M–A constituents, slender M–A constituents are easily detached from the matrix due to the lower dihedral angle-induced interfacial energy [14, 37]. Simultaneously, it is worth noting that certain types of M–A constituents are evenly distributed between acicular ferrites in the WM and polygonal ferrites in the FGHAZ, indicating a highly heterogeneous structure of brittleness–toughness phase, which can effectively suppress crack propagation [39]. However, multiple polygonal M–A constituents in the ICHAZ are continuously morphed to form a band, rendering local stress concentration, which may lower toughness in this region [28, 40].

4 Conclusions

In this work, the heterogeneous microstructure and mechanical properties of the EH420 shipbuilding steel welded joint processed by high heat input EGW were systematically studied. Major conclusions are summarized as follows:

1. Randomly interlocking distributed acicular ferrites in the WM and finely polygonal ferrites in the FGHAZ, with different crystal orientations, show a highly mixed structure, while the mutually parallel bainite laths in the CGHAZ and coarse original polygonal ferrites in the ICHAZ, with a single crystal orientation, exhibit a lowly mixed structure.
2. From the fusion line to the BM, the hardness value decreases at first from 230 HV0.5 to 185 HV0.5 and then increases until equivalent to 221 HV0.5. The heterogeneous microstructure at the junction of FGHAZ and ICHAZ undergoes a high temperature transformation from bainites to polygonal ferrites and tempered pearlites, forming a softened zone, which is the main reason for the occurrence of tensile fracture.
3. Comparing with the CGHAZ, the WM has higher toughness (129.3 J vs. 37.3 J) as it contains a large number of HAGBs and special grain boundary $\Sigma 3$ with frequencies of 79.2% and 55.28%, respectively. Moreover, coarse austenite grains in the CGHAZ and the presence of slender M–A constituents between bainite laths may likely contribute to crack propagation.

Acknowledgements This work was supported by the National Natural Science Foundation of China (Grant Nos. U20A20277, 51861130361, 51861145312, 51850410522, 5201101443, and 52011530180), the Newton Advanced Fellowship by Royal Society (Grant No. RP12G0414), the Royal Academy of Engineering (No. TSPC1070), the Special Fund for Key Program of Science and Technology of Liaoning Province (Grant No. 2019JH1/101000014), the Research Fund for Central Universities (Grant Nos. N172502004 and N2025025), the Xingliao Talents Program (Nos. XLYC1807024 and XLYC1802024), and the Regional Innovation Joint Fund of Liaoning Province (No. 2020-YKLH-39). This work is also funded in part by the National Research Foundation of South Africa (No. BRICS171211293679).

References

- [1] M. Minagawa, K. Ishida, Y. Funatsu, S. Imai, *Nippon Steel Technol. Rep.* **90**, 6 (2004)
- [2] Y. Hashiba, K. Sasaki, T. Kasuya, T. Inoue, Y. Funatsu, *Weld. World* **54**, 35 (2010)
- [3] A. Fox, M. Eakes, G. Franke, *Weld. J.* **75**, 330 (1996)
- [4] C.S. Park, Y.S. Ryu, J.S. Lee, *Adv. Mater. Res.* **26**, 495 (2007)
- [5] C. Qiu, L. Lan, D. Zhao, X. Gao, L. Du, *Acta Metall. Sin. -Engl. Lett.* **26**, 49 (2013)
- [6] X. Zou, J. Sun, H. Matsuura, C. Wang, *Metall. Mater. Trans. A* **51**, 1044 (2020)
- [7] W. Dong, M. Wen, H. Pang, S. Lu, *Acta Metall. Sin. Engl. Lett.* **33**, 391 (2019)
- [8] C.L. Davis, J.E. King, *Metall. Mater. Trans. A* **27**, 3019 (1996)
- [9] J. Hu, L. Du, J. Wang, C. Gao, *Mater. Sci. Eng. A* **577**, 161 (2013)
- [10] L. Lan, C. Qiu, D. Zhao, X. Gao, L. Du, *Mater. Sci. Eng. A* **558**, 592 (2012)
- [11] L. Lan, C. Qiu, D. Zhao, X. Gao, L. Du, *Sci. Technol. Weld. Join.* **17**, 564 (2013)
- [12] S. Lee, B.C. Kim, D. Kwon, *Metall. Mater. Trans. A* **23**, 2803 (1992)
- [13] B. Tanguy, J. Besson, R. Piques, A. Pineau, *Eng. Fract. Mech.* **72**, 49 (2005)
- [14] C. Wen, Z. Wang, X. Deng, G. Wang, R.D.K. Misra, *Steel Res. Int.* **89**, 1 (2018)
- [15] D.M. Viano, N.U. Ahmed, G.O. Schumann, *Sci. Technol. Weld. Join.* **5**, 26 (2013)
- [16] C. Liu, M. Zhao, T. Unenbayar, Y. Zhao, B. Xie, Y. Tian, Y. Shan, K. Yang, *Acta Metall. Sin. Engl. Lett.* **32**, 825 (2018)
- [17] Y. Shen, J. Leng, C. Wang, *J. Mater. Sci. Technol.* **35**, 1747 (2019)
- [18] Y. Liu, X. Wan, G. Li, Y. Wang, W. Zheng, Y. Hou, *Sci. Technol. Weld. Join.* **24**, 43 (2018)
- [19] J. Chen, C. Liu, C. Wei, Y. Liu, H. Li, *Acta Metall. Sin. Engl. Lett.* **32**, 1151 (2019)
- [20] Z. Xia, C. Wang, Y. Zhao, G. Zhang, L. Zhang, X. Meng, *Acta Metall. Sin. Engl. Lett.* **28**, 1238 (2015)
- [21] C.B. Thomson, V. Randle, *Acta Mater.* **45**, 4909 (1997)
- [22] M. Kumar, A.J. Schwartz, W.E. King, *Acta Mater.* **50**, 2599 (2002)
- [23] P. Zhou, B. Wang, L. Wang, Y. Hu, L. Zhou, *Mater. Sci. Eng. A* **722**, 112 (2018)
- [24] C. Li, Y. Wang, Y. Chen, *J. Mater. Sci.* **46**, 6424 (2011)
- [25] X. Zou, J. Sun, H. Matsuura, C. Wang, *Metall. Mater. Trans. B* **49**, 2168 (2018)
- [26] L. Lan, C. Qiu, D. Zhao, X. Gao, L. Du, *J. Mater. Sci.* **47**, 4732 (2012)
- [27] X. Di, L. Cai, X. Xing, C. Chen, Z. Xue, *Acta Metall. Sin. Engl. Lett.* **28**, 883 (2015)
- [28] X. Di, M. Tong, C. Li, C. Zhao, D. Wang, *Mater. Sci. Eng. A* **743**, 67 (2019)
- [29] S.S. Babu, *Curr. Opin. Solid St. Mater.* **8**, 267 (2004)
- [30] H.K.D.H. Bhadeshia, L.E. Svensson, B. Grefott, *Acta Metall.* **33**, 1271 (1985)
- [31] Z. Wang, X. Wang, Y. Nan, C. Shang, X. Wang, K. Liu, B. Chen, *Mater. Charact.* **138**, 67 (2018)
- [32] T.M.D. Borba, W.D. Flores, L.D.O. Turani, R.C. Junior, *Weld. Int.* **31**, 184 (2016)
- [33] Y. Wang, R. Kannan, L. Li, *Mater. Charact.* **118**, 225 (2016)
- [34] P.D. Zavattieri, H.D. Espinosa, *Acta Mater.* **49**, 4291 (2001)
- [35] X. Zou, J. Sun, H. Matsuura, C. Wang, *Metall. Mater. Trans. A* **50**, 4506 (2019)
- [36] J.S. Seo, H.J. Kim, C.H. Lee, *ISIJ Int.* **53**, 880 (2013)
- [37] C. Wen, X. Deng, Y. Tian, Z. Wang, R.D.K. Misra, *J. Mater. Eng. Perform.* **28**, 1301 (2019)
- [38] X. Wang, Z. Wang, X. Ma, S.V. Subramanian, Z. Xie, C. Shang, X. Li, *Mater. Charact.* **140**, 312 (2018)
- [39] L. Lan, C. Qiu, D. Zhao, X. Gao, L. Du, *Mater. Sci. Eng. A* **529**, 192 (2011)
- [40] Y. Wang, R. Kannan, L. Li, *Metall. Mater. Trans. A* **49**, 1264 (2018)